NANO LETTERS
Cite This: Nano Lett. 2020, 20, 1388−1395
Letter
pubs.acs.org/NanoLett

DNA Nunchucks: Nanoinstrumentation for Single-Molecule Measurement of Stiffness and Bending

Xinyue Cai,[†] D. Sebastian Arias,[†] Lourdes R. Velazquez,[†,‡] Shelby Vexler,[‡] Alexander L. Bevier,[†] and D. Kuchnir Fygenson*[,†,‡]

[†]Department of Physics, University of California, Santa Barbara, Santa Barbara, California, United States
[‡]Biomolecular Science & Engineering Program, University of California, Santa Barbara, Santa Barbara, California, United States

Supporting Information

ABSTRACT: Bending of double-stranded DNA (dsDNA) has important applications in biology and engineering, but measurement of DNA bend angles is notoriously difficult and rarely dynamic. Here we introduce a nanoscale instrument that makes dynamic measurement of the bend in short dsDNAs easy enough to be routine. The instrument works by embedding the ends of a dsDNA in stiff, fluorescently labeled DNA nanotubes, thereby mechanically magnifying their orientations. The DNA nanotubes are readily confined to a plane and imaged while freely diffusing. Single-molecule bend angles are rapidly and reliably extracted from the images by a neural network. We find that angular variance across a population increases with dsDNA length, as predicted by the worm-like chain model, although individual distributions can differ significantly from one another. For dsDNAs with phased A_6-tracts, we measure an intrinsic bend of 17 ± 1° per A_6-tract, consistent with other methods, and a length-dependent angular variance that indicates A_6-tracts are (80 ± 30)% stiffer than generic dsDNA.

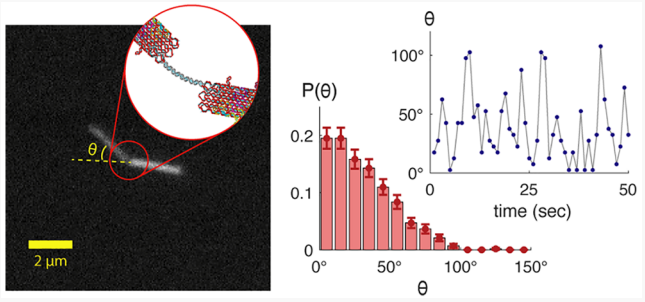

KEYWORDS: *DNA bending, persistence length, DNA origami, DNA nanotubes, A-tract*

DNA bending first excited attention in the early 1980s when the anomalous electrophoretic mobility of trypanosome kinetoplast DNA (kDNA) suggested the existence of regions of systematically bent B-DNA.[1] These bent regions were soon correlated with a striking pattern of periodically repeated $(dA)_{5-6}$ tracts separated by four to six base pairs of G+C-rich sequences.[2] Such "A-tracts" are now known to be abundant in both prokaryotes and eukaryotes and to play a role in nucleosome positioning[3] and in the regulation of transcription.[4] Around the same time, DNA bending was recognized as a common consequence of protein binding. It is now known to occur in most DNA-related biological processes.[2,5] As a result, there has been, and continues to be, great interest in characterizing both intrinsic (sequence-dependent) and induced (binding-dependent) DNA bends structurally, energetically, and dynamically.[6−8]

However, after nearly four decades of activity, rigorous characterization of the local bending of a DNA sequence remains challenging.[9,10] Gel shift electrophoresis[11] and cyclization efficiency[12] are well established and simple to perform but provide only a rough estimate of the bend angle. Nuclear magnetic resonance,[13] crystallography,[14] and X-ray scattering[15] offer excellent structural resolution but require expensive equipment, laborious sample preparation, and complex analysis procedures, and thus are impractical for routine or exploratory application. Direct visualization by atomic force microscopy (AFM)[16] and cryo-transmission electron microscopy (cryo-TEM)[17] provides good angular resolution and is increasingly accessible, but their inherent dependence on surface interactions[18] and strong 2D confinement,[19] respectively, impose biases that can be difficult to control. Finally, optically detected distance-dependent processes such as fluorescence resonant energy transfer (FRET),[20] tethered particle motion,[10] or plasmon resonance[8] can reveal bend dynamics with excellent temporal resolution but require extensive assumptions and calibration to deduce bend angles.

Here, we introduce a robust, physical method for measuring DNA bending at the single-molecule level with standard laboratory equipment, minimal sample preparation, and such simple analysis procedures so as to enable routine quantification of bend angles and bending stiffness in arbitrary DNA sequences. The method involves the self-assembly and direct visualization of "DNA nunchucks": a nanostructure consisting of a pair of tiled DNA nanotube "arms" that are grown from two cylindrical DNA origami "seeds", which are joined end-to-end by a double-stranded DNA "linker". The process and yield of DNA nunchuck assembly has been described previously.[21] Here we report design considerations for reliable nunchuck angle measurement and calibrate nunchucks for use in measuring and

Received: December 2, 2019
Revised: December 24, 2019
Published: December 24, 2019

DOI: 10.1021/acs.nanolett.9b04980
Nano Lett. 2020, 20, 1388−1395

monitoring DNA bending by studying the bend angle distributions of a variety of intrinsically bent and straight linkers (with and without A_6-tracts).

Nunchuck Design and Assembly. Nunchucks of the heterogeneous type (i.e., with different tiles in each arm) were assembled as described in Mohammed et al.[21] (Figure 1) except,

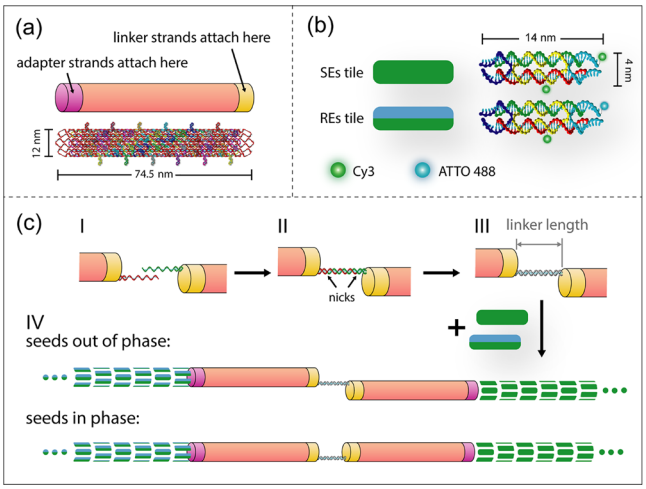

Figure 1. Nunchuck design and assembly. (a) Cylindrical DNA origami seeds, adapted from Mohammed et al.,[21] are folded from a 3024-base-long scaffold strand. Scaffold fringes provide attachment sites for a linker strand on one end of the seed (yellow) and for adapter tiles on the other (magenta). (b) Two types of fully orthogonal DAE-E tiles[23] are used to make distinguishable nanotube arms. Each SE tile carries two Cy3 fluorophores, and each RE tile carries one Cy3 and one ATTO 488. (c) Seed dimers form when linker strands hybridize (I → II). They are then ligated to seal the nicks and are purified by agarose gel electrophoresis (II → III). Pure, ligated seed dimers are added to a mixture of SE and RE tiles (III), which nucleate on their respective adapter strands and self-assemble into fluorescently distinct nanotubes, making it possible to verify the seeded nature and readily locate the linker of a nunchuck by fluorescence microscopy. The relative position of the seeds about the linker axis varies with linker length, as determined by the double-helical pitch (IV).

instead of using the 7 kb-long M13mp18 genome as a scaffold, each origami seed was folded from a 3 kb scaffold (p3024, from Nafisi et al.[22]). Because the origami design involves only 2.7 kb, using a shorter scaffold greatly reduces the amount of single-stranded DNA (ssDNA) that protrudes from the midpoint of each seed (see Figure 2 in Mohammed et al.[21]). Compaction of the ∼300-base excess had no noticeable effect on nunchuck bend angle distributions (Supplementary Note S12), suggesting that, even uncompacted, the protruding ssDNA does not influence nunchuck conformation.

Nunchucks were made with a variety of linkers of different lengths and sequences (Supplementary Note S4). Linker length is defined as the number of base pairs in the duplex DNA connecting two seeds (Figure 1c-III). Due to the helical nature of dsDNA, this length determines the relative position of the seeds about the linker axis (Figure 1c-IV). An "out-of-phase" positioning, in which the seeds are separated by a half-integer number of helical turns, reduces the possibility of steric hindrance between seeds when the linker bends and ensures that any intrinsic bends at the seed−linker junctions cancel out.

Nunchuck Imaging. To monitor and measure linker bending, nunchucks were mechanically confined to a thickness of <0.5 μm between PEG-coated glass surfaces, which left them able to diffuse freely while imaged by conventional, wide-field epi-fluorescence microscopy (see the Methods section). Using a shutter-triggered camera and an oxygen scavenging system,[24] it was possible to collect ∼2000 images of any individual nunchuck. Our frame rate was limited to 0.3 Hz $\leq f \leq$ 10 Hz, and although we were not able to definitively measure the angular decorrelation time, measures of angular diffusion and consistency upon downsampling suggested that f = ∼1 Hz sufficed to remove most correlations between frames (Supplementary Note S13).

Nunchucks chosen for imaging had arms between 2 and 6 μm long with no obvious irregularities. The location of the linker was evident in the images because one arm carried twice as many Cy3 fluorophores as the other (Figure 2a−d). Images were

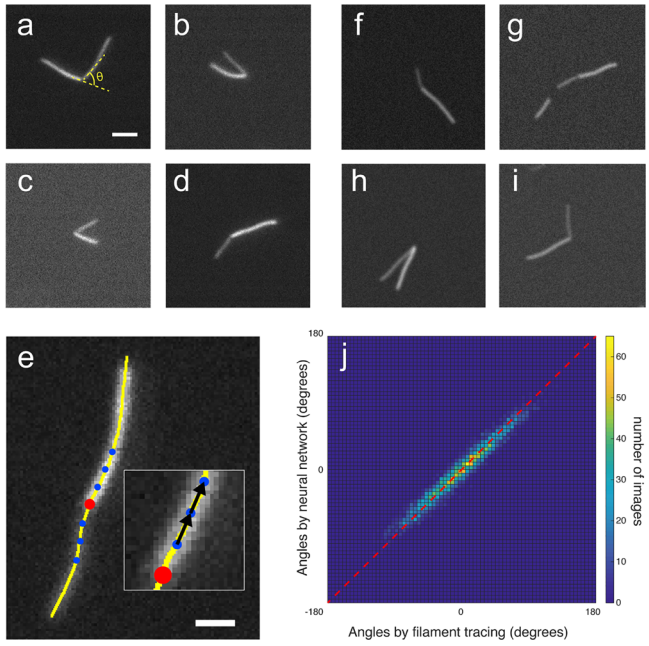

Figure 2. Raw data and bend angle analysis methods. (a−d) Example images of four different nunchucks, all at the same scale (bar = 2 μm). The nunchuck bend angle, θ, is defined to be 0° when straight and 180° when completely bent, as illustrated in part a. (e) One method of determining bend angle is based on tracing the nunchuck contour (shown in yellow) using the JFilament[25] plugin for ImageJ.[26] The vertex is identified from the discontinuity in brightness along the contour (red dot). Beginning 8 pixels from the vertex (closest blue dot), eight vectors along each arm, each 8 pixels in length and offset by 1 pixel, are used to calculate 64 dot products (the first and last vectors on the bright arm are shown as black arrows in the inset). The bend angle and its uncertainty are calculated from the average and standard deviation of the normalized dot products (bar = 2 μm). (f−i) Examples of computer-generated nunchuck images used for training the neural network. The images were designed to mimic common nonidealities of real images, including curved arms, frame-to-frame variations in contrast, and other nanotubes in random locations. (j) A confusion matrix comparing nunchuck bend angles from 5314 real nunchuck images as measured by filament analysis (horizontal) and by neural network (vertical).

enhanced for contrast, cropped to a 200 pixel × 200 pixel square centered on the bounding box containing the nunchuck, and analyzed for bend angle, θ (Figure 2a), either by filament tracing (Figure 2e), using the JFilament plug-in[25] for ImageJ,[26] or by a deep, convolutional neural network. Most bend angles reported here were extracted by the neural network because it proved significantly faster and more accurate than filament tracing. The

DOI: 10.1021/acs.nanolett.9b04980
Nano Lett. 2020, 20, 1388−1395

neural network was trained on 570,960 computer-generated images that reproduced the most common nonidealities of real images, including curved arms, frame-to-frame contrast variations, and other nanotubes near/crossing the nunchuck of interest (Figure 2f–i). A confusion matrix of bend angles extracted from images of real nunchucks shows good agreement between the two methods (Figure 2j). The slight deviation from perfect correspondence (red diagonal) reflects the filament tracing algorithm's bias toward smooth contours. Further details of neural network structure, training, performance, and application are given in Supplementary Note S11.

Bend Angle Distributions. To gauge the accuracy and precision of nunchuck-based bend angle measurements, we sampled bend angles at 1 Hz and analyzed their distributions for hundreds of individual nunchucks of various linker lengths and sequences. For each linker, we observed and analyzed at least 11 individual nunchucks (see Movies S1–S3 for examples). As an example, Figure 3 presents the bend angle histograms for 17

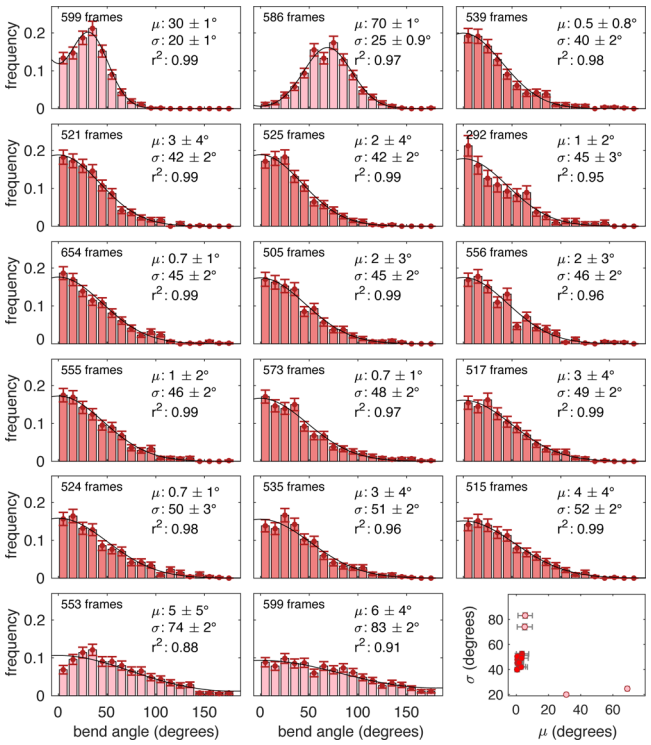

Figure 3. Bend angle histograms of nunchucks with 32-bp linkers sampled at 1 Hz. Parameters are extracted from least-squared error fits to a folded normal distribution. Uncertainties in the mean, μ, and standard deviation, σ, were determined by bootstrapping for 500 iterations at the original sample size. Histograms are sorted from top left to bottom right in order of ascending σ. At the bottom right is a scatter plot of σ vs μ for the set. Lighter shading corresponds to outliers, which were excluded from the calculation of set statistics.

individual nunchucks whose 32-bp linker contains no intrinsic bends. Note that the bend angle, θ, is defined between 0 and 180°. Each histogram is therefore fit to a folded normal distribution function with mean, μ, and standard deviation, σ (Supplementary Note S9).

A scatter plot of σ vs μ (Figure 3, bottom right) reveals an important feature typical of nunchuck data sets: while a majority of nunchucks have very similar bend angle distributions, approximately 25% (4 out of 17 in this case) either differ significantly (>2 s.d.) in μ or σ or fit poorly ($R^2 \leq 0.85$) to a folded normal distribution (Supplementary Notes S16 and S17). These outliers cannot be attributed to environmental factors or imaging artifacts, as they were often recorded at the same time and in the same field of view as the other nunchucks. They also are not the result of incomplete ligation: nunchucks with linkers redesigned to be nick-free had the majority of μ and σ values within the uncertainty of those made with only one ligatable nick (Supplementary Note S10). A likely explanation is that outliers are malformed nunchucks, with, for example, rogue strands that bridge between seeds or missing strands that compromise their structural integrity. Set statistics were therefore calculated based only on clustered distributions (i.e., excluding outliers).

Bend Angle Variance vs Linker Length. As a first test of the accuracy of nunchuck-based bend angle measurements, we looked at the dependence of angular variance, σ^2, on linker length. The observed bend angle, θ, of a nunchuck corresponds to the angle between the tangent vectors at the ends of its linker. According to the worm-like chain model,[27] the average of the cosine of this angle is related to the three-dimensional persistence length of the linker, L_p, as

$$\langle \cos\theta \rangle = e^{-\lambda/L_p} \tag{1}$$

where λ is the contour length separating the tangents. The three-dimensional persistence length applies rather than the two-dimensional one because both the linker length (<20 nm) and the nanotube diameter (~10 nm) are more than an order of magnitude smaller than the gap between PEG-passivated glass surfaces (~500 nm). This geometry allows the linker to adopt any three-dimensional conformation at no energy cost because the nunchuck is free to rotate so as to keep its arms parallel to the plane of confinement. In addition, room temperature thermal energy can induce significant twist (~50°) in a linker,[28] providing another pathway by which it can explore all bent states.

For $\theta \sim N(0, \sigma^2)$, it is well-established (see Supplementary Note S14) that

$$\langle \cos\theta \rangle = e^{-\sigma^2/2} \tag{2}$$

which, combined with eq 1, predicts a linear increase in angular variance with the effective linker length, λ:

$$\sigma^2 = \frac{2\lambda}{L_p} \tag{3}$$

Nunchuck measurements of angular variance support this prediction (Figure 4a). For linker lengths that place the seeds on opposite sides of the helical axis (Figure 4a, black circles), angular variance increases linearly with linker length, with a slope corresponding to $L_p = 131 \pm 33$ bp, consistent with other measurements on dsDNA under similar salt conditions.[29] Linker lengths that place the seeds on the same side of the helical axis (Figure 4a, red squares) fit the same line when short enough that collisions between seeds are rare (<37 bp). When linker lengths are longer, the observed angular variance is significantly suppressed, likely due to steric hindrance between the seeds. The angular variance of a linker with intermediate phasing (55 bp, blue triangle) falls between the in-phase (52 bp) and out-of-phase (58 bp) cases, accordingly.

The nonzero intercept of the linear fit indicates flexibility in the linker–seed connection. We capture this in terms of a length, l_0, by which the effective linker length, λ, exceeds the defined linker length, l, such that

DOI: 10.1021/acs.nanolett.9b04980
Nano Lett. 2020, 20, 1388–1395

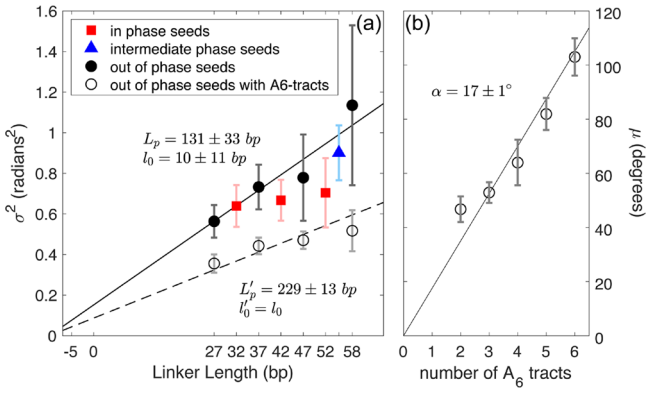

Figure 4. (a) Filled markers: weighted averages of angular variances of ≥12 individual nunchucks containing no intrinsic bend, as a function of linker length. Angular variance increases linearly with linker length, as expected (eq 3), for linker lengths that place seeds on opposite sides of the helical axis (black circles). Linker lengths that place seeds on the same side (red squares) follow the same trend if they are short but not if they are long enough to permit collisions between seeds. The angular variance of a 55-bp linker (blue triangles) lies in between those of 52-bp and 58-bp linkers, as expected. A linear fit (to black circles only) yields an estimate of the dsDNA linker persistence length, L_p, and the distance, $l_0/2$, at which the linker orientation is anchored into a seed. Error bars depict ± one (weighted) standard deviation of the angular variances. Open markers: Angular variance as a function of linker length for linkers with the highest possible density of phased A_6-tracts. Data are fit to eq 3 with $l'_0 \equiv 10$ bp (based on l_0), yielding $L'_p = 229 \pm 13$ bp. (b) Mean of the bend angle distribution, μ, as a function of the number of phased A_6-tracts, N, in the linker. For $N = 3$, μ is the weighted average of data from 27-, 37-, and 47-bp linkers. For $N = 2$, 4, 5, 6, data were taken with a single linker length of 37, 37, 47, and 58 bp, respectively. The linear fit $\mu = N\alpha$ yields an intrinsic bend angle of $\alpha = 17 \pm 1°$ per A_6-tract.

$$\lambda = l + l_0 \tag{4}$$

The observation that $l_0 = 10 \pm 11$ bp is consistent with the linker's bend penetrating about half a helical turn into each of the flanking seeds. Alternatively, it can be interpreted as resulting from flexibility intrinsic to the linker−seed junction.

A_6-Tract Bend Angle and Stiffness. Having thus calibrated the effective linker length and established the reliability of nunchuck angular variance measurements for linkers that place seeds out of phase, we used such linkers to measure the mean bend angle, μ, as a function of the number of intrinsically bent, appropriately phased A_6-tracts[30] (Supplementary Note S4) (Figure 4b). Fitting the data to a line with zero intercept, $\mu = N\alpha$, where N is the number of A_6-tracts in the linker, yields $\alpha = 17 \pm 1°$, in good agreement with, and comparable precision to, previous measurements (reviewed by Stellwagen et al.[31]).

Interestingly, angular distributions of nunchucks with A_6-tract-laden linkers had significantly lower variances than those without (Figure 4a). For example, 37-bp linkers with no A_6-tracts had a standard deviation of 49 ± 4°, while 37-bp linkers with three A_6-tracts had a standard deviation of 41 ± 3° (Supplementary Table S10). To determine whether this effect is due to the presence of A_6-tracts or a result of, say, steric hindrance suppressing angular variance, we also looked at 37-bp linkers with three A_6-tracts phased so as to result in no net bend angle. These had a mean bend angle of 0 ± 1° and a standard deviation of 43 ± 5° (Supplementary Table S10), similar to that of the intrinsically bent 37-bp linkers with three A_6-tracts.

While A_6-tracts are expected to be stiffer than generic dsDNA,[31−33] to our knowledge, their stiffness has never before been determined experimentally. Comparing linkers of different lengths and similar (highest possible) densities of phased A_6-tracts (27 bp with $N = 3$, 37 bp with $N = 4$, 47 bp with $N = 5$, and 58 bp with $N = 6$) and fitting to eq 3 using $l'_0 = l_0 = 10$ bp determined using unbent linkers (Figure 4a), we find $L'_p = 229 \pm 13$ bp, an increase of (80 ± 30)% compared to generic dsDNA.

Distinct Distributions from Identical Nunchucks. Nunchuck bend angle distributions, being derived from single molecules, contribute insights that summary statistics cannot provide. In particular, we note that, even after excluding outliers on the basis of clustering, identically prepared nunchucks often exhibited distinct bend angle distributions. For example, among nunchucks with A_6-tracts in their linkers (Figure 5), every set of

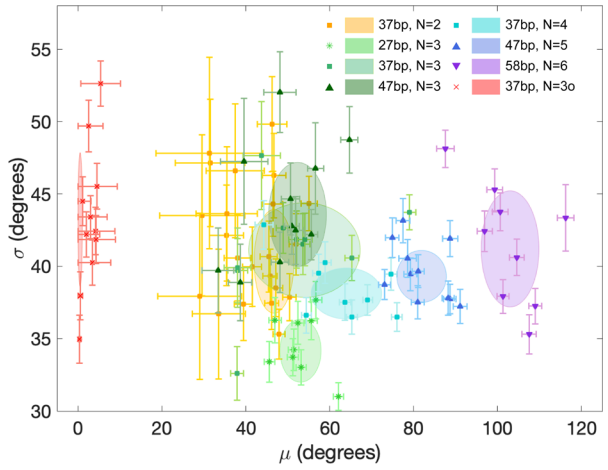

Figure 5. Scatter plot of σ and μ values of all individual nunchucks containing A_6-tracts. Color distinguishes linkers with different numbers of A_6-tracts; shade and marker shape distinguish linkers of different lengths. An ellipse of the corresponding color and shade is centered on the weighted averages of μ and σ for the set, and its horizontal and vertical radii represent the weighted standard deviations of μ and σ, respectively.

nunchucks with a given linker contained at least one pair (and often several) whose bend angle distributions differed significantly ($p \ll 1/N_{pairs}$, per the Kolmogorov−Smirnov test). Such distinct histograms can arise if linkers have metastable bent states that occur only rarely and which are therefore variably sampled in different image sequences (typically <20 min duration). One time series in particular provided a clear indication that such rare, metastable bent states occur. In it, a nunchuck with a 58-bp nominally straight linker switched multiple times between a highly bent state and a less bent, possibly unbent, state (Supplementary Note S17, Movie S4).

Thus, while the linker length dependence of nunchuck bend angle variance provides a direct measure of short dsDNA stiffness that is consistent with the persistence length of long dsDNA (Figure 4a), clustered but distinguishable bend angle histograms from identically prepared nunchucks suggest that linkers access rare, metastable bent states (i.e., kinks) even at room temperature. These results help explain why some experiments observe high cyclization rates among short (<70 bp) dsDNAs[34−37] while others find no discrepancy with the measured stiffness of longer dsDNA.[38−40]

DOI: 10.1021/acs.nanolett.9b04980
Nano Lett. 2020, 20, 1388−1395

Limitations. The range of linker lengths we explored was relatively narrow, 27 bp < l < 58 bp. It was bounded on the lower end by thermal stability of the base-pairing that secured the linker to the seeds and on the upper end by cost. Nunchucks with shorter linkers can be assembled by redesigning the linker strands so as to place the nicks within the seeds (Supplementary Figure S4b). Nunchucks with longer linkers are readily made, but once a linker is longer than its persistence length, the diminished correlation between its ends' orientations and the increased probability for collisions between the nunchucks arms will complicate interpretation of bend angle histograms.

Another limitation of nunchuck measurements comes from the degeneracy of the folded normal fitting function when both μ and σ are unknown and $0° < \mu \lesssim \sigma$ (Supplementary Note S9), in which case the fitting has poor resolution in μ and σ. This limitation can be overcome by concatenating coplanar motifs, so as to push μ into the resolvable range, or by redesigning the nanotube arms to be permanently kinked or branched,[41] so as to prevent in-plane rotations about the double-helical axis. The latter would enable unambiguous measurement of $-180° \leq \theta \leq 180°$, resulting in bend angle histograms that could be fit to normal rather than folded normal distributions.

Prospects. The DNA nunchuck is a new instrument that makes single-molecule measurement of DNA bending accessible to any lab equipped for conventional fluorescence video microscopy. In this work, we establish key aspects of nunchuck design by characterizing thermally excited bend angle fluctuations as a function of linker length. Chief among these is a constraint that linker length be a half-integer number of helical turns, so that nanotube seeds extend from opposite sides of the double-helix, "out of phase" with one another. We also take an important step in validating nunchuck bend angle measurements by characterizing the intrinsic bend of phased A_6-tracts, a structure that has been investigated by numerous established techniques. Nunchuck measurements reproduced the A_6-tract bend angle known from prior studies and revealed that phased A_6-tracts have a persistence length of 229 ± 13 bp, equivalent to 76 ± 4 nm. To the best of our knowledge, this is the first experimental measurement of A_6-tract stiffness. That this persistence length is (80 ± 30)% greater than the persistence length we measured for A_6-tract-free dsDNA is roughly consistent with recent molecular dynamics simulations, which report an ∼25% enhancement.[32] Overall, our results indicate that out-of-phase nanotube arms do not significantly perturb a linker's structure and demonstrate the utility of monitoring single molecules' bend angle fluctuations.

As the A_6-tract measurements demonstrate, the nunchuck is easily adapted to characterize the sequence-dependent stiffness and bending of dsDNA. Structural anomalies, such as single-stranded gaps, locally melted bubbles, and unpaired bulges, can also be probed. Indeed, nunchucks can be used to study bending of any molecular structure that can be incorporated within a linker.[42] With the advent of commercially available RNA−DNA chimeric oligomers, we anticipate nunchuck-based measurement of RNA motifs such as three-way or four-way junctions,[43,44] right angles (RA),[45] and kissing loops[46] will usefully refine parameters used in simulation and prediction of RNA[47] and origami[48] nanostructures.

Although the range of linker lengths we tested was limited, it is nevertheless large enough to accommodate most sequence-specific protein binding sites, opening the possibility of using nunchucks to study binding-induced DNA bending. Such measurements will be especially interesting because of the unique combination of structural (angular) and dynamic (stiffness, kinetic) information nunchucks provide. On several occasions, we observed a nunchuck change >100° in a matter of seconds (Supplementary Note S17, Movie S4). This suggests that, despite the hydrodynamic drag on the nanotube arms (3.3 and 4.2 μm in that particular case), nunchucks can have sufficient temporal resolution to report on the lifetimes of induced bends that persist for more than a few seconds.[8,49]

Overall, our results establish DNA nunchucks as an attractive system for studying dsDNA bending at the single-molecule level. They offer mean bend angle determination with few-degree resolution, just like conventional approaches, along with significant advantages, including measures of bend stiffness via bend angle variance and direct dynamical observation, and a lower barrier to adoption. Hence, the DNA nunchuck approach is well positioned to become a standard technique for the study of functionally relevant bending of dsDNA and any molecules to which it can be rigidly attached.

Methods. *Materials.* The P3024 scaffold was produced and provided by Parsa Nafisi and Shawn Douglas, UCSF.[22] DNA strands for staples, linkers, adapters, and tiles were synthesized by Integrated DNA Technologies, Inc. (www.idtdna.com). Staple strands and guard strands were purchased purified by standard desalting. Linker and adapter strands were purchased HPLC purified when size permitted and PAGE purified otherwise. Tile strands were purchased PAGE purified. Concentrations of purified strands were confirmed by Nanodrop 2000c using absorbance at 260 nm based on extinction coefficients quoted by the manufacturer.

Linker Kination. Linker strands were kinated individually at a concentration of 2.5 μM in a solution containing 10 units of T4 polynucleotide kinase (New England Biolabs, M0201L) and 1× T4 DNA ligase buffer (New England Biolabs, B0202S) by incubating at 37 °C for 2 h. The solution was then heated to 90 °C for 10 min to deactivate the kinase and diluted to 100 nM for use in seed mixtures.

Seed Formation. Seed design and strand sequences are given in Supplementary Notes S1−S3. Linker design and sequences are given in Supplementary Note S4. Seed monomers with complementary linkers were annealed separately (Supplementary Note S5) and then dimerized by mixing equal volumes and incubating at 31 °C for at least 12 h. Dimerized seeds were ligated for 2 h at room temperature with 20 nM T4 DNA ligase (New England Biolabs, M0202L), 0.5 nM extra ATP in 1× T4 DNA ligase buffer supplemented with 1× TAE-Mg buffer (40 mM Tris base, 20 mM acetic acid, 1 mM EDTA, pH 8.2, with 12.5 mM magnesium acetate). Then, 100 μL/mL of proteinase K (VWR, 470179-306) was added and the solution was incubated at 37 °C for 1 h to inactivate the ligase.

Seed Purification. Seed dimers were purified away from excess staples, proteins, monomers, etc., by agarose gel electrophoresis. Slab gels made of 1 wt % agarose (EXCLUSIEVE, High Resolution Agarose) in gel-running buffer (1× TAE-Mg) with 0.5 μg/mL ethidium bromide were loaded with 60 μL of ligated seed dimers and run at 90 V for 1 h in an ice bath (Supplementary Note S6). Seed dimers, which ran slower than seed monomers, were cut out and extracted using Freeze N Squeeze DNA Gel Extraction Spin Columns (Bio-Rad, 7326166), and then, they were stored at room temperature and used within 2 weeks.

Nunchuck Formation. RE and SE tile strands were mixed in equimolar ratios and slowly annealed from 90 to 31 °C, with a brief pause at 40 °C during which seed dimers were added.

DOI: 10.1021/acs.nanolett.9b04980
Nano Lett. 2020, 20, 1388−1395

Detailed recipes can be found in Supplementary Note S5. The SE and RE tile strand sequences were the same as those in Rothemund et al.[23] Because the nunchuck arm lengths and overall yield (ratio of nunchucks to spontaneously nucleated nanotubes) depend sensitively on the seed-to-tile ratio, for every nunchuck preparation, a series of seed dimer dilutions were used. Each was briefly imaged to determine the best mixture for bend angle imaging (typically arm lengths of 2−4 μm and ∼50% yield). Samples consisted of 3 μL of 6× diluted mix placed between an 18 mm × 18 mm no. 1 coverslip and a glass slide (both uncleaned) and sealed with candle wax.

Glass Cleaning. Glass slides (3 in. × 1 in., Spectrum, 451-82010-R6) and coverslips (22 mm × 22 mm, Fisherfinest, 12548B) were loaded into staining racks (6817B, Newcomer Supply; 50949462, Electron Microscopy Sciences) sitting in glass jars and sonicated for 10 min in pure water (Milli-Q A10, Millipore) containing 0.1 vol % of concentrated cleaning solution (Micro-90, International Products Corp). Slides and slips were then rinsed five times with pure water (by filling the glass jars with water and gently shaking to remove soap residue). Both slides and slips were then incubated in 2 M NaOH for 30 min to etch away a thin layer of glass and again rinsed five times with pure water to remove the remaining NaOH. Finally, they were rinsed once in pure ethanol to remove water from the surfaces (for faster drying), placed in a 50 °C oven to dry, and stored in glass jars.

Glass Passivation. A 300 μL portion of ethanol, 3 μL of glacial acetic acid, and 2.5 mg of mPEG-silane (Laysan Bio) were mixed and heated for 5 min at 50 °C to dissolve mPEG-silane, which would not otherwise be soluble in ethanol. A 15 μL portion of this solution was placed on a clean coverslip, which was quickly flipped onto the center of a clean slide so that the solution completely filled the gap between the slide and the slip. The slide−slip pair was then stored horizontally in a tightly sealed 50 mL centrifuge tube (Falcon, 14-432-22) containing 5 mL of ethanol at room temperature, the vapor of which prevents the mPEG-silane solution from drying. Slide−slip pairs were ready for use after 3 days and remained usable for at least 2 months.

Sample Preparation. PEG-coated slides and slips were removed from Falcon tubes, separated, and incubated in ethanol at 60 °C for 20 min to rinse away unreacted mPEG-silane. The glass pieces were then blow-dried with nitrogen, reassembled with PEG surfaces in contact, and pressed against each other in a home-built jig (Supplementary Note S8). While under pressure in the jig, the coverslip was glued to the slide with UV-curing nail polish (Gelixir, top coat) along all edges but leaving two small openings on opposite sides to form a flow cell. After curing under UV LEDs (SUNUV, SUN9C) for 60 s, the flow cell was removed from the jig and loaded with sample (see below). "Guard" strands,[21] designed to inhibit nanotube nucleation and growth during room-temperature imaging, were sometimes added to the sample immediately before bend angle imaging but were discovered to be unnecessary and omitted from the protocol (Supplementary Note S12). When used, 0.1 μL of guard strands (initially at 4 μM) was added to 1 μL of nunchuck sample and allowed to sit for 1 min at 31 °C. A PCA-trolox oxygen scavenging system (OSS)[24] was added to the sample immediately before loading to reduce bleaching of fluorescent molecules during imaging (Supplementary Note S18). A 0.6 μL portion of the nunchuck−OSS mixture was dropped onto one opening of a freshly prepared flow cell and allowed to spread between the slide and the slip by capillary action. When the solution reached the opposite opening, any remaining liquid was wiped away with a kimwipe and both openings were sealed with candle wax. The process of filling the flow cell reduced the apparent yield of nunchucks significantly. Typical flow-cell samples contained 1 nunchuck for every 10 nanotubes (Supplementary Note S7).

Imaging. Samples were imaged in epi-fluorescence mode on an inverted microscope (Olympus, IX70) with a 100×/1.30 oil immersion objective and a Cooke Sensicam QE camera. The fluorescence optics for Cy3 were 325AF45 (excitation), 560DRLP (dichroic), and HQ610/75 (emission), and those for Atto 488 were 475DF40 (excitation), 505DRLP (dichroic), and HQ535/50 (emission). Nunchucks selected for imaging had (1) arms between 2 and 4 μm long with no obvious irregularities, (2) relatively few other tubes around, (3) freedom to move and bend in the field of view, and (4) consistently sharp focus throughout. Images were taken with a time delay of either 1 or 3 s between frames. The exposure time per frame was typically 10 ms, but it was increased when the nunchuck was imaged for long enough for bleaching to become noticeable (>1000 frames). While it was easy to collect ∼2000 images of any individual nunchuck, image sequences were typically limited to ∼700 frames to maximize the number of sequences taken before nunchucks degraded due to mechanical torsion or lower magnesium concentrations. Otherwise, imaging typically stopped when the nunchuck showed signs of degradation (breaks or kinks in the arms) or stuck to another structure (tube or nunchuck) or the glass surface.

■ ASSOCIATED CONTENT

Supporting Information

The Supporting Information is available free of charge at https://pubs.acs.org/doi/10.1021/acs.nanolett.9b04980.

Nunchuck design, sequences, and assembling protocol (S1−S5), sample agarose gel for seed purification (S6), nunchuck yield (S7), the jig design (S8), the folded normal distribution function (S9), effect of linker nicks (S10), the neural network and comparison to filament analysis (S11), effects of protocol and design variations (S12 and S15), angular diffusion coefficient and decorrelation time (S13), a proof of relation between θ and σ for Gaussian-distributed θ (S14), all bend angle results (S16), outlier exclusion (S17), a detailed oxygen scavenging system protocol (S18), and a table of all set statistics (S19) (PDF)

Movie S1, a sample nunchuck movie (post-cropping) (AVI)

Movie S2, a sample nunchuck movie (post-cropping) (AVI)

Movie S3, a sample nunchuck movie (post-cropping) (AVI)

Movie S4, a sample nunchuck movie (post-cropping) (AVI)

■ AUTHOR INFORMATION

Corresponding Author

*E-mail: deborah@physics.ucsb.edu.

ORCID

Xinyue Cai: 0000-0002-4051-7413

D. Kuchnir Fygenson: 0000-0002-5681-3938

DOI: 10.1021/acs.nanolett.9b04980
Nano Lett. 2020, 20, 1388−1395

Author Contributions

X.C. performed research, analyzed data, and wrote the paper. D.S.A. conceived and implemented the training image generator, developed the neural network, and characterized its performance. L.R.V. defined initial protocols and collected and processed data. S.V. and A.B. collected and processed data. D.K.F. designed research, wrote the paper, and supervised all aspects.

Notes

The authors declare no competing financial interest.

■ ACKNOWLEDGMENTS

The authors thank P. Nafisi and S. Douglas for the generous gift of P3024, H. Tran for the generous gift of gel nail top coat and a UV LED curing lamp, P. W. K. Rothemund and T. Liedl for discussions, and S. Ji for computing resources and help. This work was supported by UCSB start up funds and private donor funds. Use was made of computational facilities purchased with funds from the National Science Foundation (CNS-1725797) and administered by the Center for Scientific Computing (CSC). The CSC is supported by the California NanoSystems Institute and the Materials Research Science and Engineering Center (MRSEC; NSF DMR 1720256) at UC Santa Barbara. Both D.S.A. and L.R.V. received funding from the California Alliance for Minority Participation (CAMP) sponsored by the Louis Stokes Alliances of the National Science Foundation. S.V. received funding from the Early Undergraduate Research and Knowledge Acquisition (EUREKA) program through the UC Santa Barbara Office of the Executive Vice Chancellor. Both S.V. and A.L.B. received an Undergraduate Research and Creative Activities (URCA) grant from the UCSB College of Letters and Sciences.

■ REFERENCES

(1) Marini, J. C.; Levene, S. D.; Crothers, D. M.; Englund, P. T. Bent Helical Structure in Kinetoplast DNA. *Proc. Natl. Acad. Sci. U. S. A.* **1982**, *79*, 7664−7668.
(2) Wu, H.-M.; Crothers, D. M. The Locus of Sequence-Directed and Protein-Induced DNA Bending. *Nature* **1984**, *308*, 509.
(3) Kaplan, N.; Moore, I. K.; Fondufe-Mittendorf, Y.; Gossett, A. J.; Tillo, D.; Field, Y.; Leproust, E. M.; Hughes, T. R.; Lieb, J. D.; Widom, J.; Others. The DNA-Encoded Nucleosome Organization of a Eukaryotic Genome. *Nature* **2009**, *458*, 362.
(4) Iyer, V.; Struhl, K. Poly(dA:dT), a Ubiquitous Promoter Element That Stimulates Transcription via Its Intrinsic DNA Structure. *EMBO J.* **1995**, *14*, 2570−2579.
(5) Swinger, K. K.; Rice, P. A. IHF and HU: Flexible Architects of Bent DNA. *Curr. Opin. Struct. Biol.* **2004**, *14*, 28−35.
(6) Maher, L. J. Mechanisms of DNA Bending. *Curr. Opin. Chem. Biol.* **1998**, *2*, 688−694.
(7) Privalov, P. L.; Dragan, A. I.; Crane-Robinson, C. The Cost of DNA Bending. *Trends Biochem. Sci.* **2009**, *34*, 464−470.
(8) Reinhard, B. M.; Sheikholeslami, S.; Mastroianni, A.; Alivisatos, a. P.; Liphardt, J. Use of Plasmon Coupling to Reveal the Dynamics of DNA Bending and Cleavage by Single EcoRV Restriction Enzymes. *Proc. Natl. Acad. Sci. U. S. A.* **2007**, *104*, 2667−2672.
(9) Gietl, A.; Grohmann, D. Modern Biophysical Approaches Probe Transcription-Factor-Induced DNA Bending and Looping. *Biochem. Soc. Trans.* **2013**, *41*, 368−373.
(10) Brunet, A.; Chevalier, S.; Destainville, N.; Manghi, M.; Rousseau, P.; Salhi, M.; Salomé, L.; Tardin, C. Probing a Label-Free Local Bend in DNA by Single Molecule Tethered Particle Motion. *Nucleic Acids Res.* **2015**, *43*, e72−e72.
(11) Lane, D.; Prentki, P.; Chandler, M. Use of Gel Retardation to Analyze Protein-Nucleic Acid Interactions. *Microbiol. Mol. Biol. Rev.* **1992**, *56*, 509−528.
(12) Crothers, D. M.; Drak, J.; Kahn, J. D.; Levene, S. D. *Methods in Enzymology*; Elsevier: 1992; Vol. *212*, pp 3−29.
(13) Macdonald, D.; Herbert, K.; Zhang, X.; Polgruto, T.; Lu, P. Solution Structure of an A-tract DNA Bend. *J. Mol. Biol.* **2001**, *306*, 1081−1098.
(14) Nelson, H. C.; Finch, J. T.; Luisi, B. F.; Klug, A. The Structure of an Oligo(dA)·oligo(dT) Tract and Its Biological Implications. *Nature* **1987**, *330*, 221.
(15) Shi, X.; Beauchamp, K. A.; Harbury, P. B.; Herschlag, D. From a Structural Average to the Conformational Ensemble of a DNA Bulge. *Proc. Natl. Acad. Sci. U. S. A.* **2014**, *111*, E1473−E1480.
(16) Rivetti, C.; Walker, C.; Bustamante, C. Polymer Chain Statistics and Conformational Analysis of DNA Molecules with Bends or Sections of Different Flexibility. *J. Mol. Biol.* **1998**, *280*, 41−59.
(17) Bednar, J.; Furrer, P.; Katritch, V.; Stasiak, A.; Dubochet, J.; Stasiak, A. Determination of DNA Persistence Length by Cryo-Electron Microscopy. Separation of the Static and Dynamic Contributions to the Apparent Persistence Length Of DNA. *J. Mol. Biol.* **1995**, *254*, 579−594.
(18) Heenan, P. R.; Perkins, T. T. Imaging DNA Equilibrated onto Mica in Liquid Using Biochemically Relevant Deposition Conditions. *ACS Nano* **2019**, *13*, 4220−4229.
(19) Destainville, N.; Manghi, M.; Palmeri, J. Microscopic Mechanism for Experimentally Observed Anomalous Elasticity of DNA in Two Dimensions. *Biophys. J.* **2009**, *96*, 4464−4469.
(20) Woźniak, A. K.; Schröder, G. F.; Grubmüller, H.; Seidel, C. A.; Oesterhelt, F. Single-Molecule FRET Measures Bends and Kinks in DNA. *Proc. Natl. Acad. Sci. U. S. A.* **2008**, *105*, 18337−18342.
(21) Mohammed, A.; Velazquez, L.; Chisenhall, A.; Schiffels, D.; Fygenson, D.; Schulman, R. Self-assembly of precisely defined DNA nanotube superstructures using DNA origami seeds. *Nanoscale* **2017**, *9*, 522−526.
(22) Nafisi, P. M.; Aksel, T.; Douglas, S. M. Construction of a Novel Phagemid to Produce Custom DNA Origami Scaffolds. *Synth. Biol.* **2018**, *3*, ysy015.
(23) Rothemund, P. W.; Ekani-Nkodo, A.; Papadakis, N.; Kumar, A.; Fygenson, D. K.; Winfree, E. Design and Characterization of Programmable DNA Nanotubes. *J. Am. Chem. Soc.* **2004**, *126*, 16344−16352.
(24) Aitken, C. E.; Marshall, R. A.; Puglisi, J. D. An Oxygen Scavenging System for Improvement of Dye Stability in Single-Molecule Fluorescence Experiments. *Biophys. J.* **2008**, *94*, 1826−1835.
(25) Smith, M. B.; LI, H.; Shen, T.; Huang, X.; Yusuf, E.; Vavylonis, D. Segmentation and Tracking of Cytoskeletal Filaments Using Open Active Contours. *Cytoskeleton* **2010**, *67*, 693−705.
(26) Schindelin, J.; Arganda-Carreras, I.; Frise, E.; Kaynig, V.; Longair, M.; Pietzsch, T.; Preibisch, S.; Rueden, C.; Saalfeld, S.; Schmid, B.; et al. Fiji: An Open-Source Platform for Biological-Image Analysis. *Nat. Methods* **2012**, *9*, 676.
(27) Doi, M.; Edwards, S. F. *The Theory of Polymer Dynamics*; Oxford University Press: 1988; Vol. *73*.
(28) Strick, T.; Bensimon, D.; Croquette, V. Micro-Mechanical Measurement of the Torsional Modulus of DNA. *Genetica* **1999**, *106*, 57−62.
(29) Lu, Y.; Weers, B.; Stellwagen, N. C. DNA Persistence Length Revisited. *Biopolymers* **2002**, *61*, 261−275.
(30) Haran, T. E.; Mohanty, U. The Unique Structure of A-tracts and Intrinsic DNA Bending. *Q. Rev. Biophys.* **2009**, *42*, 41−81.
(31) Stellwagen, E.; Peters, J. P.; Maher, L. J., Iii; Stellwagen, N. C. DNA A-tracts Are Not Curved in Solutions Containing High Concentrations of Monovalent Cations. *Biochemistry* **2013**, *52*, 4138−4148.
(32) Mitchell, J. S.; Glowacki, J.; Grandchamp, A. E.; Manning, R. S.; Maddocks, J. H. Sequence-Dependent Persistence Lengths of DNA. *J. Chem. Theory Comput.* **2017**, *13*, 1539−1555.

DOI: 10.1021/acs.nanolett.9b04980
Nano Lett. 2020, 20, 1388−1395

(33) Nikolova, E. N.; Bascom, G. D.; Andricioaei, I.; Al-Hashimi, H. M. Probing sequence-specific DNA flexibility in A-tracts and pyrimidine-purine steps by nuclear magnetic resonance ^{13}C relaxation and molecular dynamics simulations. *Biochemistry* **2012**, *51*, 8654−8664.
(34) Cloutier, T. E.; Widom, J. Spontaneous Sharp Bending of Double-Stranded DNA. *Mol. Cell* **2004**, *14*, 355−362.
(35) Wiggins, P. A.; Van Der Heijden, T.; Moreno-Herrero, F.; Spakowitz, A.; Phillips, R.; Widom, J.; Dekker, C.; Nelson, P. C. High Flexibility of DNA on Short Length Scales Probed by Atomic Force Microscopy. *Nat. Nanotechnol.* **2006**, *1*, 137−141.
(36) Yuan, C.; Chen, H.; Lou, X. W.; Archer, L. A. DNA bending stiffness on small length scales. *Phys. Rev. Lett.* **2008**, *100*, 018102.
(37) Vafabakhsh, R.; Ha, T. Extreme bendability of DNA less than 100 base pairs long revealed by single-molecule cyclization. *Science* **2012**, *337*, 1097−1101.
(38) Wang, H.; Milstein, J. N. Simulation Assisted Analysis of the Intrinsic Stiffness for Short DNA Molecules Imaged with Scanning Atomic Force Microscopy. *PLoS One* **2015**, *10*, No. e0142277.
(39) Schöpflin, R.; Brutzer, H.; Müller, O.; Seidel, R.; Wedemann, G. Probing the elasticity of DNA on short length scales by modeling supercoiling under tension. *Biophys. J.* **2012**, *103*, 323−330.
(40) Mastroianni, A. J.; Sivak, D. A.; Geissler, P. L.; Alivisatos, A. P. Probing the conformational distributions of subpersistence length DNA. *Biophys. J.* **2009**, *97*, 1408−1417.
(41) Jorgenson, T. D.; Mohammed, A. M.; Agrawal, D. K.; Schulman, R. Self-Assembly of Hierarchical DNA Nanotube Architectures with Well-Defined Geometries. *ACS Nano* **2017**, *11*, 1927−1936.
(42) de Rochambeau, D.; Sun, Y.; Barlog, M.; Bazzi, H. S.; Sleiman, H. F. Modular Strategy to Expand the Chemical Diversity of DNA and Sequence-Controlled Polymers. *J. Org. Chem.* **2018**, *83*, 9774−9786.
(43) Lescoute, A.; Westhof, E. Topology of three-way junctions in folded RNAs. *RNA* **2006**, *12*, 83−93.
(44) Hohng, S.; Wilson, T. J.; Tan, E.; Clegg, R. M.; Lilley, D. M. J.; Ha, T. Conformational Flexibility of Four-Way Junctions in RNA. *J. Mol. Biol.* **2004**, *336*, 69−79.
(45) Grabow, W. W.; Zhuang, Z.; Swank, Z. N.; Shea, J.-E.; Jaeger, L. The right angle (RA) motif: a prevalent ribosomal RNA structural pattern found in group I introns. *J. Mol. Biol.* **2012**, *424*, 54−67.
(46) Réblová, K.; Špačková, N.; Šponer, J. E.; Koča, J.; Šponer, J. Molecular dynamics simulations of RNA kissing−loop motifs reveal structural dynamics and formation of cation-binding pockets. *Nucleic Acids Res.* **2003**, *31*, 6942−6952.
(47) Lipfert, J.; Skinner, G. M.; Keegstra, J. M.; Hensgens, T.; Jager, T.; Dulin, D.; Köber, M.; Yu, Z.; Donkers, S. P.; Chou, F.-C.; et al. Double-Stranded RNA Under Force and Torque: Similarities to and Striking Differences from Double-Stranded DNA. *Proc. Natl. Acad. Sci. U. S. A.* **2014**, *111*, 15408−15413.
(48) Sharma, R.; Schreck, J. S.; Romano, F.; Louis, A. A.; Doye, J. P. K. Characterizing the motion of jointed DNA nanostructures using a coarse-grained model. *ACS Nano* **2017**, *11*, 12426−12435.
(49) Skoko, D.; Wong, B.; Johnson, R. C.; Marko, J. F. Micromechanical Analysis of the Binding of DNA-Bending Proteins HMGB1, NHP6A, and HU Reveals Their Ability To Form Highly Stable DNA-Protein Complexes. *Biochemistry* **2004**, *43*, 13867−13874.

DOI: 10.1021/acs.nanolett.9b04980
Nano Lett. 2020, 20, 1388−1395